Coherent Control and Suppressed Nuclear Feedback of a Single Quantum Dot Hole Qubit

Kristiaan De Greve, Peter L. McMahon, and David Press
E. L. Ginzton Laboratory, Stanford University, Stanford, California 94305, USA

Thaddeus D. Ladd* and Yoshihisa Yamamoto
E. L. Ginzton Laboratory, Stanford University, Stanford, California 94305, USA and
National Institute of Informatics, Hitotsubashi 2-1-2, Chiyoda-ku, Tokyo 101-8403, Japan

Dirk Bisping, Christian Schneider, Martin Kamp, Lukas Worschech, and Alfred Forchel
Technische Physik, Physikalisches Institut, Wilhelm Conrad Röntgen Research Center for
Complex Material Systems, Universität Würzburg, Am Hubland, D-97074 Würzburg, Germany

Sven Höfling
E. L. Ginzton Laboratory, Stanford University, Stanford, California 94305, USA and
Technische Physik, Physikalisches Institut, Wilhelm Conrad Röntgen Research Center for
Complex Material Systems, Universität Würzburg, Am Hubland, D-97074 Würzburg, Germany

Future communication and computation technologies that exploit quantum information require robust and well-isolated qubits. Electron spins in III-V semiconductor quantum dots, while promising candidates, see their dynamics limited by undesirable hysteresis and decohering effects of the nuclear spin bath. Replacing electrons with holes should suppress the hyperfine interaction and consequently eliminate strong nuclear effects. Using picosecond optical pulses, we demonstrate coherent control of a single hole qubit and examine both free-induction and spin-echo decay. In moving from electrons to holes, we observe significantly reduced hyperfine interactions, evidenced by the reemergence of hysteresis-free dynamics, while obtaining similar coherence times, limited by non-nuclear mechanisms. These results demonstrate the potential of optically controlled, quantum dot hole qubits.

The coherence of quantum bits (qubits) is crucial for the implementation of quantum computation and communication schemes [1]. Electron spins in III-V semiconductor quantum dots, among the fastest, most promising qubits, see their coherent dynamics limited by strong hyperfine interactions with the nuclear spin bath [2–6]. Dynamical decoupling, the repeated application of rotation pulses to decouple a qubit from a noise bath, has been applied to the electron-nuclear hyperfine interaction, and was shown to increase the coherence of a single electron spin [7]. Unfortunately, electron-nuclear spin bath dynamics are highly non-Markovian [8–11], a cumbersome feature which complicates the control operations required for effective dynamical decoupling, and which affects the fidelity of control operations [8]. Isotopic engineering may also reduce nuclear noise. While this is possible for quantum dots or charged impurities in group-IV or group II-VI semiconductors [1], III-V semiconductor compounds do not possess stable spin-zero isotopes. The strong electron-spin contact hyperfine interaction, however, can be avoided by engineering qubits based on valence-band holes [12–15], as the symmetry of the hole wavefunction leaves only the weak residual dipolar interaction as the leading term in the hyperfine Hamiltonian [13].

Electrons and holes are not completely equivalent, but as we show here, they can be controlled by the same methods. The large heavy-hole (HH)-light-hole (LH) splitting in III-V QDs makes it possible to consider only the HH manifolds, especially at low temperatures. The HHs can be described in a pseudo-spin-1/2 formalism [12], with a perturbative treatment of LH inmixing. The p-like symmetry of the hole Bloch wavefunction enables more spin-orbit coupling mechanisms than for an electron spin [12], especially in the case of significant HH-LH mixing [16]. The hole-spin decoherence is therefore more sensitive to electric fields and orbital degrees of freedom than that of electron spins. We nevertheless confirm in this work that the physical mechanisms underpinning optical initialization and ultrafast optical control of hole qubits are essentially identical to those of electron spins [17, 18], and allow for an arbitrary single-qubit rotation to be performed in several tens of picoseconds. This is in contrast to RF and microwave control of hole qubits: there, the coupling of a single HH with the control field is significantly lower than that of an electron spin [19], resulting in orders of magnitude slower control operations. Alternatives such as the use of LH spins (through strain engineering of III-V heterostructures), exchange coupling between HH spins in a double
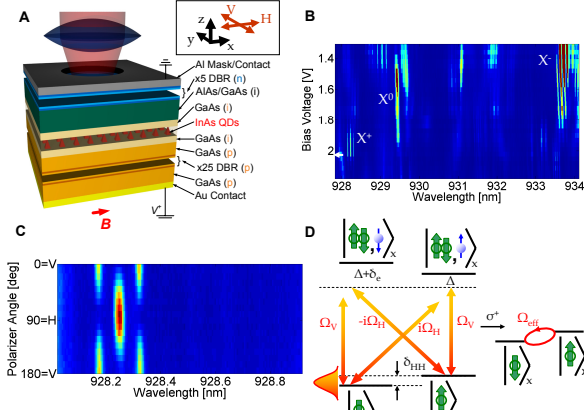
FIG. 1: (**A**) Sample structure and geometry used (not to scale). A single layer of quantum dots is embedded in a p-i-n-diode, and separated from a hole reservoir by a 25 nm tunnel barrier. A 110 nm AlAs/GaAs superlattice prevents tunneling from an electron reservoir. Distributed Bragg Reflector pairs (DBR, 5 pairs on top and 25 pairs on the bottom) form a low-Q cavity. We isolate a single QD through spatial and spectral filtering. A magnetic field B is applied along the x-axis (Voigt geometry), and a bias voltage V^+ determines the charge state of the QD. Inset: orientation (x,z) and polarization convention (H,V) used. (**B**) Magnetophotoluminescence plot ($B = 6$ T; above-band pumping, $\lambda = 785$ nm) of a QD used in the experiment, as a function of the bias voltage. X^+ indicates the hole-charged trion state, X^- the optical-excitation induced, electron-charged trion, and X^0 the neutral exciton state. The white arrow indicates the bias voltage used in Fig. 1c. (**C**) Polarization dependence of the X^+ photoluminescence when biased at 2.0 V ($B = 6$ T). Note that two of the four X^+-emission lines overlap at this magnetic-field strength, leading to the apparent increase in brightness of the center lines. (**D**) Level structure with idealized polarization selection rules, as used in the experiment. Applying a detuned broadband laser pulse ($\Delta/2\pi = 340$ GHz, 3.67 ps FWHM) generates an effective coupling between the HH-states (Ω_{eff}). For an 8 T magnetic field, $\delta_{\mathrm{HH}}/2\pi = 30.2$ GHz, $\delta_{\mathrm{e}}/2\pi \sim 35$ GHz.

QD, or all-electrical QD-molecule HH spin g-tensor control have been proposed [19, 20], though have yet to be implemented.

We systematically studied coherent single-hole manipulation in several QDs in multiple devices, using two different types of device structures (charge-tuneable and hole-δ-doped [21]). The results from different QDs and devices are qualitatively equivalent, although quantitative measurements do yield different values from dot to dot. All figures in this Report result from one particular charge-tuneable QD, which we deterministically charge with a hole by embedding it in a p-i-n-diode (Fig. 1**A**) - an approach similar to the one used in Refs. 22,14,15. We bias the diode so as to load a single hole into the QD, which we detect optically through magneto-photoluminescence (Fig. 1**B**). A magnetic field is applied in Voigt geometry (perpendicular to the opti-

cal axis, Fig. 1**A**), giving rise to a double Λ-system under optical excitation (Figs. 1**C** and **D**). Previous work on electron spins [17, 18] demonstrated the coherent and ultrafast manipulation of such a Λ-system with circularly polarized, detuned, picosecond pulses. We employ a similar ultrafast coherent manipulation scheme for the HH in our QD (Fig. 2**A**). A magnetic field of 8 T splits the HH eigenstates $|\Downarrow\rangle$ and $|\Uparrow\rangle$ by the pseudo-spin Larmor frequency $\delta_{\mathrm{HH}}/2\pi = 30.2$ GHz. Before applying any rotation pulses, we initialize the hole qubit by optical pumping [6, 14, 23, 24], for which we use the hole-trion state ($|\Downarrow\Uparrow,\uparrow\rangle$, consisting of a HH singlet and an unpaired electron spin). A 26 ns narrowband continuous wave (CW)-laser pulse (1-2 MHz linewidth before modulation) is applied resonant with the $|\Uparrow\rangle$-$|\Downarrow\Uparrow,\downarrow\rangle$-transition, which initializes the hole spin into the $|\Downarrow\rangle$-state in a few ns. The same CW-laser pulse sequence is used for reading out the hole spin state. If, after initialization, the coherent manipulation pulse rotates the spin into the $|\Uparrow\rangle$-state, then the subsequent optical-pumping pulse will cause a single photon to be emitted from the $|\Downarrow\Uparrow,\uparrow\rangle$-$|\Downarrow\rangle$-transition. This photon is filtered, and subsequently detected by a single-photon counter. For coherent manipulation, we use broadband pulses (FWHM: 3.67 ps) from a modelocked laser, detuned by $\Delta/2\pi = 340$ GHz. A combination of electro-optic modulators, beamsplitters and variable-delay paths (Fig. 2**B**) allows accurate control over the timing of the pulses [21].

The effect of a single rotation pulse is outlined in Fig. 2**C**. The rotation pulse effectively couples the $|\Downarrow\rangle$ and $|\Uparrow\rangle$-states, which can be equivalently interpreted as implementing a stimulated Raman transition [18, 25] or as the result of an AC-Stark-shift [17]. For a fixed rotation pulse duration, Rabi oscillations between $|\Downarrow\rangle$ and $|\Uparrow\rangle$ are observed as a function of the rotation pulse power.

The Rabi oscillations demonstrate single qubit rotations around the z-axis (Fig. 1**A** shows the axis conventions used). However, arbitrary qubit control requires controlled rotation about a second axis. For this, we use the effective Larmor precession of the HH pseudo-spin around the magnetic-field axis (x-axis). This precession can be probed through Ramsey interferometry. In Fig. 2**D**, the resulting Ramsey fringes are shown when two $\pi/2$ pulses are applied with a variable delay τ. From the Ramsey fringe visibility, a fidelity of 0.945 can be deduced for a single $\pi/2$ rotation. Any arbitrary single qubit rotation can be performed by decomposition into rotations about the x- and z-axes [18]. This is illustrated in Fig. 2**E**, where the entire Bloch sphere surface is explored by sweeping through both the z-rotation angle (θ) and x-rotation angle ($\delta_{\mathrm{HH}}\tau$). Using these methods, any single qubit rotation can be performed in approximately 20 ps or less [18].

The complete SU(2) control of a QD spin allows for the observation of hyperfine interactions between the spin and the nuclei. Nuclear spin interactions manifest them-
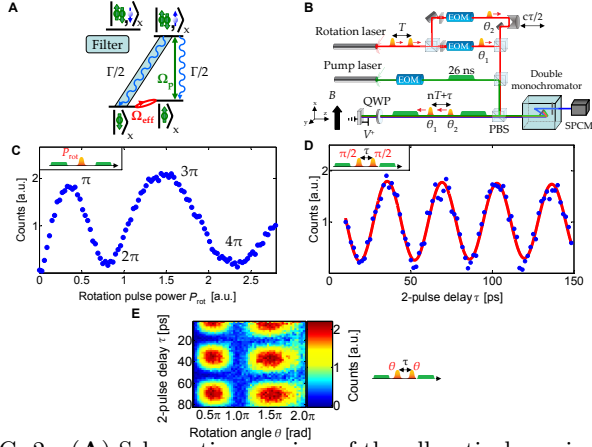
FIG. 2: (**A**) Schematic overview of the all-optical manipulation scheme. Γ: spontaneous emission rate from the $|\Downarrow\Uparrow,\downarrow\rangle$-state, estimated at $(1\text{ ns})^{-1}$; Ω_p: coupling due to the optical pumping/readout laser; Ω_{eff}: effective Rabi-coupling resulting from the detuned modelocked-laser pulses. (**B**) Experimental setup. The ML-laser pulses (period: $T = 13$ ns) are split into two independently adjustable (power, delay τ) branches, allowing for multiple rotation laser pulses to be applied sequentially. A double monochromator is used to filter out the scattered laser light. QWP: quarterwave plate; PBS: polarizing beamsplitter; EOM: electro-optic modulator; SPCM: single photon counting module; V^+: bias voltage; B: external magnetic field. (**C**) Coherent Rabi oscillations. When varying the power P_{rot} of the rotation pulses, the HH-spin state coherently evolves from $|\Downarrow\rangle$ to $|\Uparrow\rangle$ and back, resulting in an oscillatory photon count signal. Inset: the timing of the initialization/readout pulses (green) and rotation pulse (red). (**D**) Ramsey interference fringes. After a first $\pi/2$ rotation pulse, the hole spin is allowed to precess around the external magnetic field (Larmor precession, $\omega_L/2\pi = 30.2$ GHz). By delaying a second $\pi/2$ pulse by an amount τ, Ramsey fringes are observed. Inset: timing of the initialization/readout and rotation pulses. (**E**) Demonstration of complete SU(2) control of the single hole qubit. By changing both the delay τ and the pulse rotation angle θ, the entire surface of the Bloch sphere is explored. Inset: timing and pulse amplitude used.

selves primarily as Overhauser shifts of the effective magnetic field. These cause both dephasing of qubit memory and angle errors in single qubit control. In principle, compensation methods exist for static Overhauser shifts, but such shifts change over time, and unfortunately their dynamics have been shown to depend on previously applied control operations. For electron spins in single QDs, such non-Markovian, hysteretic behavior was observed in both Ramsey interferometry [11] and in continuous-wave (CW) laser scans [9, 10]. A suppressed hyperfine interaction for a hole qubit should show an absence of these effects, and allow for easy implementation of accurate x-rotations in arbitrary pulse sequences.

In Figs. 3**A** and **B**, we compare the analogs of free-induction decay (FID) for a single electron spin and a hole pseudo-spin through Ramsey interferometry [11]. For a single electron spin, the resulting Ramsey fringes are
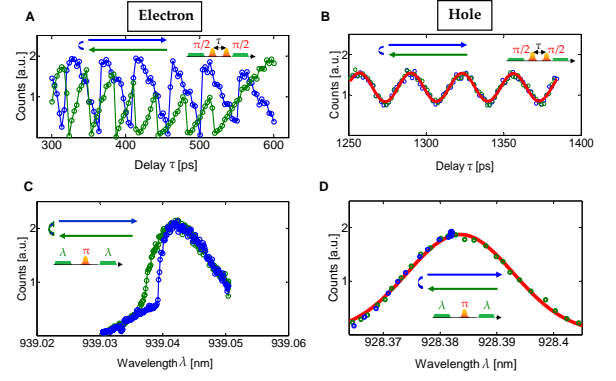

FIG. 3: (**A**) Asymmetric and hysteretic Ramsey fringes for an electron spin in a QD. The green and blue circles refer respectively to backwards and forwards scanning of the delay line, as indicated by the arrows [11]. Inset: the pulse sequence used in the experiment. (**B**) Symmetric and hysteresis-free Ramsey fringes for a hole spin in a QD. Even for large delays, the Ramsey fringes remain perfectly sinusoidal. The green and blue circles refer to different scanning directions, as indicated by the arrows. The red curve represents a sinusoidal least-squares fit. Inset: pulse sequence used. (**C**) Effective absorption signal for an electron spin in a QD, showing clear asymmetry and hysteresis upon scanning the pump laser wavelength in different directions (green and blue circles, as indicated by the arrows). Inset: pulse sequence used. (**D**) Effective absorption signal for a hole spin in a QD. No hysteresis or asymmetry was observed upon scanning in different directions (green and blue circles, as indicated by the arrows). Red curve: least-squares fit of a Gaussian absorption profile. Inset: pulse sequence used.

shown in Fig. 3**A**, using experimental parameters similar to those reported previously [11]. For these experiments, the nuclear spin polarization is significantly altered during each optical pumping cycle. Since the nuclear polarization affects the electron spin's coherent evolution, a strong feedback loop develops, resulting in the observed hysteretic behavior [10, 11]. For a HH qubit, shown in Fig. 3**B**, no such hysteresis was observed. This lack of observable hysteresis is understood to be due to the reduction of Overhauser shifts that results from the absence of a contact hyperfine coupling for holes. We observe a reduction of least 30 in the nuclear feedback strength when using holes instead of electrons, in line with recent direct measurements of the reduced hyperfine coupling of holes [26, 27]. This estimate is a conservative lower bound, limited by hole decoherence that may obscure possible weak effects [21].

We also performed experiments in which we scan the optical pumping laser while applying a π-rotation pulse (inset of Figs. 3**C** and **D**). This mimics two-CW-laser resonant absorption experiments performed for electrons [9, 10] and for holes [15, 26]. For electron spins, multiple experiments [9–11] report that scanning the
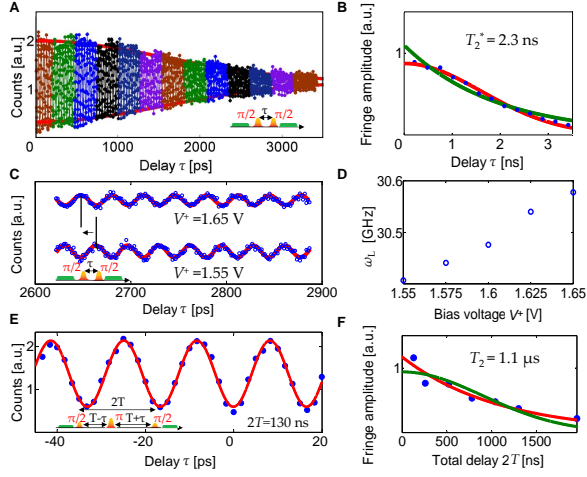
FIG. 4: (**A**) Ramsey fringes as a function of the delay τ between two $\pi/2$ pulses. The different colors refer to different positions of the stage on the rail (see text), while the red envelopes indicate a least-squares-fit Gaussian decay with $T_2^* = 2.3$ ns. Inset: pulse timing used. (**B**) Amplitude of the Ramsey fringes, as a function of the delay τ. Red curve: fit to a Gaussian decay ($T_2^* = 2.3$ ns); green curve: fit to an exponential decay. (**C**) Long-delay Ramsey fringes, for different applied voltage bias V^+. Top: $V^+ = 1.65$ V; bottom: $V^+ = 1.55$ V. Red curves: least-squares, sinusoidal fit. The cumulative effect of the difference in Larmor precession frequency ω_L can be seen in the shifting of the curves. (**D**) Larmor-precession frequency ω_L as a function of the externally applied bias voltage V^+. (**E**) Spin-echo fringes as a function of fine-delay τ, for a total delay $2T = 130$ ns. Red curve: fit to a sinusoid. Inset: pulse timing used. (**F**) Spin-echo fringe amplitude as a function of the total delay $2T$. Red curve: fit to exponential decay ($T_2 = 1.1\mu$s); green curve: fit to Gaussian decay.

laser through the $|\downarrow\rangle$-$|\downarrow\uparrow, \Uparrow\rangle$-resonance leads to a hysteretic nuclei-induced wandering of that resonance; this effect is seen in Fig. 3**c**. In contrast, no hysteresis is observed for a hole-charged QD (Fig. 3**D**). The absorption profile is completely symmetric, and is best fit by a Gaussian (red curve in Fig. 3**D**) with a linewidth of 6.7 GHz. The notable broadening suggests significant spectral diffusion of our hole-charged QD. For different dots, as well as for measurements on the δ-doped sample, we obtain comparable linewidths, typically 3 times larger than for similar, electron-doped QDs when measured in the same setup. Similar broadening of hole-charged QDs has been observed previously [15].

A qubit's coherence is characterized by both T_2^*, which results from very low frequency noise, and by T_2, which characterizes decoherence due to higher frequency noise [1]. T_2^* is found as the decay of the time-averaged hole-pseudo-spin FID, as shown in Fig. 4**A**. In Fig. 4**B** the fringe height is shown as a function of the delay between the pulses. The decay is best fit by a Gaussian (i.e., $\propto \exp[-(t/T_2^*)^2]$) with $T_2^* = 2.3$ ns, and is independent of

the magnetic field for fields between 6 and 10 T. It is unlikely that nuclear spin effects are responsible for the T_2^* times we observe. Theoretical calculations of the FID of a single hole predict much longer time-averaged dephasing times when limited by hyperfine interactions, even when taking finite HH-LH mixing into account [13, 28]. Non-nuclear dephasing processes are far more likely; such processes limit coherence in localized hole spins in quantum wells [16, 29], and may even overwhelm nuclear processes in electron-charged quantum dots at some magnetic fields, depending on the dot's proximity to noisy surface states [6]. These dephasing processes generally arise from fluctuations in the localizing potential, a process that may be observed as spectral diffusion of the optical transitions, evidenced by the optical linewidth in the resonance-scanning experiment described above.

The effect of spectral diffusion on hole spin coherence, in the form of randomly varying electric fields, can be directly examined in our sample. By deliberately changing the electrical bias over the QD, corresponding to spectral shifts similar in magnitude to those presumedly responsible for spectral diffusion, we measure notably different effective Larmor precession frequencies of the HH pseudo-spin. In Fig. 4**C**, the cumulative effect of such a difference in Larmor frequency is shown through long-delay Ramsey fringes. The different precession frequencies lead to anti-phase Ramsey fringes for delays similar to T_2^*. In Fig. 4**D**, the monotonic increase of the Larmor frequency with applied bias is shown. These results indicate that electrical fields couple strongly to the spin coherence, and that T_2^* is actually limited by electric field fluctuations rather than nuclear hyperfine effects. We investigated possible sample-dependent effects by repeating the same experiments on different QDs, with similar results. In addition, similar values for T_2^* were obtained for the QDs in the δ-doped sample [21].

Our measurement of T_2^* contrasts markedly with an estimate of T_2^* obtained via coherent population trapping in similar HH-doped QDs [15]. However, that experiment effectively filters a hole precession process for one particular spectral location, removing the potential dephasing effects of spectral diffusion. Consequently, substantially longer values of T_2^* are reported, possibly corresponding to the onset of nuclear-induced dephasing.

While the ability of electric fields to shift the effective QD Larmor frequency may unfortunately impact T_2^*, it simultaneously provides a convenient advantage of hole pseudo-spin qubits over electron-spin qubits: namely, it introduces the ability to locally tune multiple qubits into resonance, which may have important implications for viable two-qubit gates, and aid in scalability to many-qubit systems.

Finally, we use a spin-echo technique [6] for measuring the T_2-decoherence time of the HH qubit. Fig. 4**E** illustrates the fringes obtained from scanning the π-echo-pulse, and Fig. 4**F** shows the fringe contrast as a function

of total delay $2T$. The decay is best fit by an exponential (i.e., $\propto \exp[-(t/T_2)]$), with $T_2 = 1.1$ μs, the same order of magnitude as for electron spins [6]. Here as well, magnetic-field-dependent studies do not show any dependence on the field between 6 and 10 T. In combination with a single-qubit operation time of about 20 ps, this T_2-value allows for approximately 50,000 operations within the coherence time of the qubit. Although 500 times longer than T_2^*, the obtained T_2-value is still lower than what is theoretically expected for a nuclear-spin-limited decay. Phonon interactions are expected to only weakly affect the quantum dot hole spin [12, 13, 30], and can therefore also be excluded as a dominant source of decoherence. In addition, T_1 in our experiment, while limited by leakage of the optical pump laser, was measured to be at least 1 to 2 orders of magnitude larger [21]. It therefore appears that T_2 is limited by a similar, non-nuclear mechanism as that which most likely limits T_2^*, i.e. charge-induced spectral diffusion. Such a process can be mimicked by AC-modulation of the external voltage bias, and we have indeed observed a suppression of T_2 when introducing such a modulation. We measured significant dot-to-dot variance of T_2, sometimes measuring T_2 as low as several hundred ns. The variation is likely due to differences in the spin-orbit contribution to the hole-pseudospin Hamiltonian, in large part due to different HH-LH mixing for dots of different shapes and levels of strain. Further understanding the decoherence mechanisms for holes may enable extension of the spin coherence through further device engineering, as well as through the application of advanced dynamical decoupling schemes, as have recently been demonstrated for electron spins [7].

In conclusion, we experimentally confirm the recent theoretical predictions [12, 13, 28] of the weak interactions of III-V QD hole spins with the nuclear bath. Our experiments also show that ultrafast coherent control techniques work with high fidelity for hole qubits, resulting in coherence times comparable to those for electron spins, and that complex nuclear spin bath dynamics no longer measurably affect the qubit. However, further study of non-nuclear decoherence mechanisms is required to fully exploit the promise of QD holes as qubits.

———————

* Currently at HRL Laboratories, LLC, 3011 Malibu Canyon Rd., Malibu, CA 90265, USA

[1] T. D. Ladd, F. Jelezko, R. Laflamme, Y. Nakamura, C. Monroe, and J. L. O'Brien, Nature **464**, 45 (2010).
[2] W. A. Coish and D. Loss, Phys. Rev. B **70**, 195340 (2004).
[3] J. R. Petta et al., Science **309**, 2180 (2005).
[4] W. Yao, R.-B. Liu, and L. J. Sham, Phys. Rev. B **74**, 195301 (2006).
[5] W. M. Witzel and S. Das Sarma, Phys. Rev. B **74**, 035322 (2006).
[6] D. Press, K. De Greve, P. McMahon, T. D. Ladd, B. Friess, C. Schneider, M. Kamp, S. Hfling, A. Forchel, and Y. Yamamoto, Nat. Photonics **4**, 367 (2010).
[7] H. Bluhm, S. Foletti, I. Neder, M. Rudner, D. Mahalu, V. Umansky, and A. Yacoby, Nat. Phys. **7**, 109 (2011).
[8] I. T. Vink et al., Nat. Phys. **5**, 764 (2009).
[9] C. Latta et al., Nat. Phys. **5**, 758 (2009).
[10] X. Xu et al., Nature **459**, 1105 (2009).
[11] T. D. Ladd, D. Press, K. De Greve, P. McMahon, B. Friess, C. Schneider, M. Kamp, S. Höfling, A. Forchel, and Y. Yamamoto, Phys. Rev. Lett. **105**, 107401 (2010).
[12] D. V. Bulaev and D. Loss, Phys. Rev. Lett. **95**, 076805 (2005).
[13] J. Fischer, W. A. Coish, D. V. Bulaev, and D. Loss, Phys. Rev. B **78**, 155329 (2008).
[14] B. D. Gerardot et al., Nature **451**, 441 (2008).
[15] D. Brunner, B. D. Gerardot, P. A. Dalgarno, G. Wst, K. Karrai, N. G. Stoltz, P. M. Petroff, and R. J. Warburton, Science **325**, 70 (2009).
[16] Y. G. Semenov, K. N. Borysenko, and K. W. Kim, Phys. Rev. B **66**, 113302 (2002).
[17] J. Berezovsky, M. H. Mikkelson, N. G. Stoltz, L. A. Coldren, and D. D. Awschalom, Science **320**, 349 (2008).
[18] D. Press, T. D. Ladd, B. Zhang, and Y. Yamamoto, Nature **456**, 218 (2008).
[19] D. Sleiter and W. F. Brinkman, Phys. Rev. B **74**, 153312 (2006).
[20] R. Roloff, T. Eissfeller, P. Vogl, and W. Pötz, New J. Phys. **12**, 093012 (2010).
[21] See Supporting Online Material.
[22] R. J. Warburton, C. Schäflein, D. Haft, F. Bickel, A. Lorke, K. Karrai, J. M. Garcia, W. Schoenfeld, and P. M. Petroff, Nature **405**, 926 (2000).
[23] M. Atatüre et al., Science **312**, 551 (2006).
[24] X. Xu, Y. Wu, B. Sun, Q. Huang, J. Cheng, D. G. Steel, A. S. Bracker, D. Gammon, C. Emary, and L. J. Sham, Phys. Rev. Lett. **99**, 097401 (2007).
[25] S. E. Economou, L. J. Sham, Y. Wu, and D. G. Steel, Phys. Rev. B **74**, 205415 (2006).
[26] P. Fallahi, S. T. Yilmaz, and A. Imamoglu, Phys. Rev. Lett. **105**, 257402 (2010).
[27] E. A. Chekhovich, A. B. Krysa, M. S. Skolnick, and A. I. Tartakovskii, Phys. Rev. Lett. **106**, 027402 (2010).
[28] J. Fischer and D. Loss, Phys. Rev. Lett. **105**, 266603 (2010).
[29] M. Syperek, D. R. Yakovlev, A. Greilich, J. Misiewicz, M. Bayer, D. Reuter, and A. D. Wieck, Phys. Rev. Lett. **99**, 187401 (2007).
[30] D. Heiss, S. Schaeck, H. Huebl, M. Bichler, G. Abstreiter, J. J. Finley, D. V. Bulaev, and D. Loss, Phys. Rev. B **76**, 241306(R) (2007).
[31] This work was supported by NICT, NSF CCR-08 29694, NIST 60NANB9D9170, Special Coordination Funds for Promoting Science and Technology, the State of Bavaria, and by the JSPS through its FIRST Program. PLM acknowledges support as a David Cheriton Stanford Graduate Fellow.

Supporting Online Material for Coherent Control and Suppressed Nuclear Interaction of a Single Quantum Dot Hole Qubit: Materials and Methods

Kristiaan De Greve,[1] Peter L. McMahon,[1] David Press,[1] Thaddeus D. Ladd,[1,2,*]

Dirk Bisping,[3] Christian Schneider,[3] Martin Kamp,[3] Lukas Worschech,[3]

Sven Höfling,[1,3] Alfred Forchel,[3] and Yoshihisa Yamamoto[1,2]

[1]*E. L. Ginzton Laboratory, Stanford University, Stanford, California 94305, USA*

[2]*National Institute of Informatics, Hitotsubashi 2-1-2, Chiyoda-ku, Tokyo 101-8403, Japan*

[3]*Technische Physik, Physikalisches Institut, Wilhelm Conrad*

Röntgen Research Center for Complex Material Systems,

Universität Würzburg, Am Hubland, D-97074 Würzburg, Germany

—————
*Currently at HRL Laboratories, LLC, 3011 Malibu Canyon Rd., Malibu, CA 90265, USA

S.1. DEVICE DESIGN

Two different types of samples were studied: δ-doped samples, and charge-tuneable devices. The δ-doped samples contain about 1.5×10^{10} cm^{-2} self-assembled quantum dots, and the charge-tuneable samples about 7×10^9 cm^{-2}. For both types of samples, the quantum dots were grown using the Stranski-Krastanov method. The In flushing and partial capping technique used during the QD growth [S1] leads to the formation of flattened QDs, with an approximate height of 2 nm, and a base length of $\sim$25 nm. The detailed layer structures are provided in Fig. SI-1. For both types of samples, the QDs are embedded in a planar microcavity, consisting of Distributed Bragg Reflector (DBR) mirrors. The top and bottom mirrors consist of 5 and 25 pairs of AlAs/GaAs $\lambda/4$ layers respectively. The resulting quality factor is around 200, and helps both in increasing the signal strength (directing the emitted light upward) and reducing the noise (enabling the use of lower laser power, and therefore
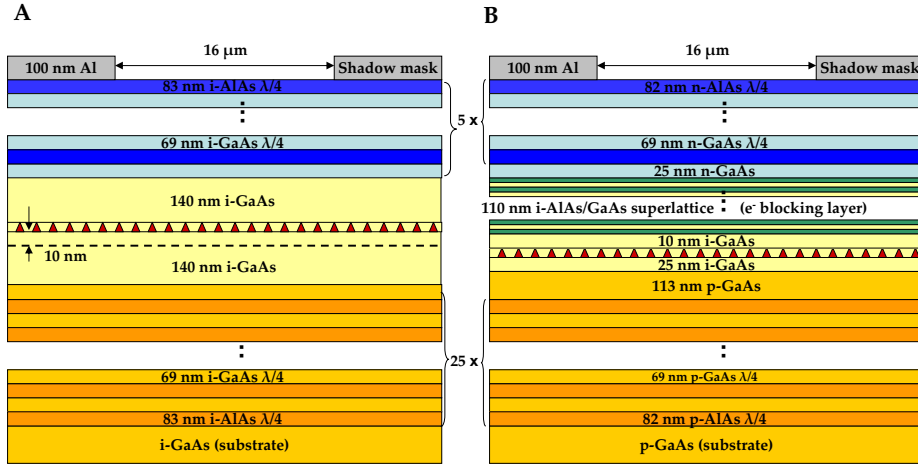

Figure S1: **Detailed layer structure.** (**A**) Detailed layer structure of the δ-doped samples. The δ-doping layer (dashed line) is located 10 nm below the quantum dots. (**B**) Detailed layer structure of the charge-tuneable devices used in the hole spin experiment. Two DBR layer stacks form an asymmetric cavity, in which a p-i-n-diode is embedded. QDs (brown triangles) are in tunnel contact (25 nm i-GaAs) with a hole reservoir. The bias voltage is applied over the Al shadow mask, and a bottom contact (not shown).

reducing the noise due to scattered laser light).

For the δ-doped samples, a carbon δ-doping layer is used, located 10 nm below the QDs. The δ-doping concentration is approximately 1.2×10^{11} cm^{-2}, and leads to a fraction of
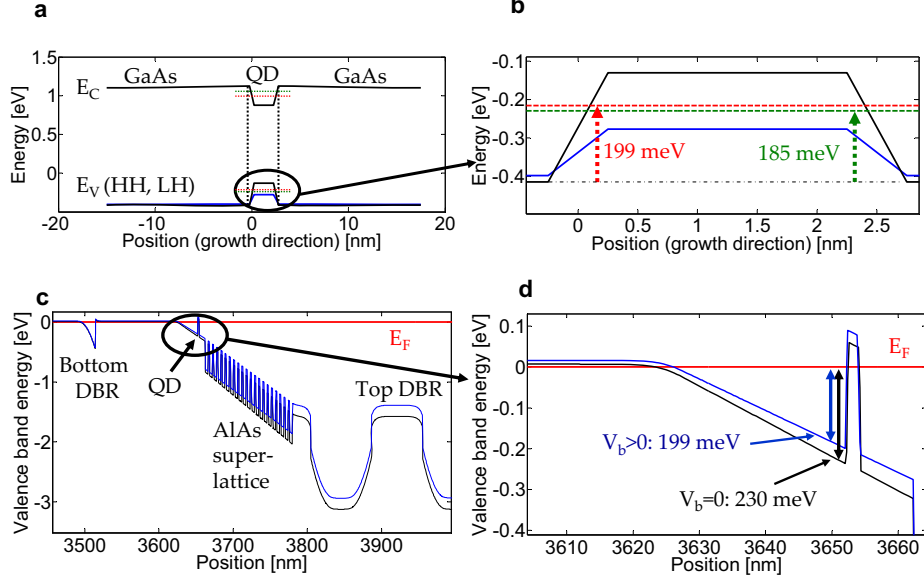

Figure S2: **Band line-up.** (**A**) Calculated energy structure (3D) of the InAs QD. E$_{C,V}$ are the conduction and valence bands respectively (the latter is calculated for the heavy (HH, black) and light hole (LH, blue) subbands). The two most tightly bound energy states in the conduction and valence bands are indicated by the red and green dashed lines. (**B**) Zoomed-in version of **A**. A flattened QD was assumed, with 2 nm height, 25 nm base length, and up to 50 % In-Ga intermixing. The most tightly bound HH state is located 199 meV above the GaAs valence band, and the second-highest state is split off by $\sim$14 meV. (**C**) Band line-up for zero (black) and positive (blue) bias (note that only the p-i-n-diode region is shown, not the entire DBR microcavity). E$_F$: Fermi-level. (**D**) Zoomed-in version of **C**: for zero applied bias, the GaAs valence band lies 230 meV below the Fermi-level, and the most tightly bound HH state therefore lies below the Fermi-level. For a positive bias, the offset between the Fermi-level and the GaAs valence band is reduced; when this offset equals the 199 meV separation with the most tightly bound HH state, resonant tunneling can result in hole-charging of the QD.

3

the QDs being charged with a single hole; we perform magneto-PL measurements in order to identify those QDs that are charged. For the charge-tuneable samples, deterministic charging occurs by embedding the QDs into a p-i-n-diode structure. The bottom DBR, as well as part of the cavity, is p-doped ($\geq 10^{18}$ cm^{-3}), while the top DBR is n-doped ($\geq 10^{18}$ cm^{-3}). The i-layer consists of two parts: a 25 nm i-GaAs layer acting as a tunnel barrier between the QDs and the p-layer [S2, S3], and a 120 nm layer separating the QDs from the n-contact. Inside the latter, we incorporated a 110 nm i-AlAs/GaAs superlattice (20 layers) to prevent charging from the n-layer [S3]. A back contact (not shown) allows for biasing of the substrate, while a metal shadow mask also serves as a contact to the n-doped layer. Apertures in the metal mask provide optical access to the QDs, at the expense of a reduced net bias over the QDs: given the relatively large width of the metal mask apertures (16 μm), the exact bias over a QD depends on the lateral position of that QD within the aperture shadow. In particular, for QDs near the center of the aperture, part of the applied bias voltage will result in a resistive voltage drop inside the n-layer, reducing the net bias over the QD. In addition, Schottky-barrier effects at the metal mask-DBR interface further reduce the effective QD bias for a given applied bias voltage.

We calculated the band structure and energy levels of the QD in a full three-dimensional simulation, using the 3D simulation tool nextnano [S4]. The results are shown in Figs. SI-2 **A** and **B**. We assume an InAs QD with an approximate height of 2 nm, and a base length of 25 nm, and account for a finite amount of In-Ga intermixing. The resulting QD emission wavelength is around 940 nm. The two most tightly bound states in both the conduction band (electron charging) and valence band (hole charging) were calculated and are indicated by the red and green dashed lines. We calculated both the HH and LH subbands, though the HH band is by far the most important. The two most tightly bound HH states in the QD are separated by ∼14 meV, and are located 199 meV above the GaAs valence band.

Next, the band structure of the charge-tuneable devices was calculated – see Figs. SI-2 **C** and **D**. Without externally applied bias, the built-in diode voltage leads to a band bending (black curve), where the hole Fermi-level is located ∼230 meV above the GaAs valence band right at the position of the QD. In order to keep our calculations tractable, we split the problem into two subproblems: a full 3D calculation of the band line-up of the QD HH bound states, and a 1D calculation of the band bending of the entire device. Hence, without applied bias, the HH QD states are located below the Fermi-level, making hole

charging of the QD energetically unfavorable. At some positive bias, the offset between the Fermi-level and the HH QD state vanishes (blue curve), with resonant tunneling allowing for deterministic charging of the QD. Numerically, this bias voltage is around 200 mV, though we emphasize that this is the real bias over the p-i-n-diode near the QD, which is often less than the applied voltage between the device contacts, especially for QDs located near the center of the mask aperture (DC Stark shifts and Schottky-barrier effects account for an additional offset). Pauli- and Coulomb-blockade effects subsequently lead to a stable voltage plateau where single-hole charging is possible.

In view of the relatively large QD density, about 50 QDs were located within our diffraction-limited laser spot (charge-tuneable devices; for the δ-doped samples, some 150 QDs), and several of those were resonant with the microcavity. Their spectral inhomogeneity allows us to identify a single quantum dot. In Fig. 1 **B** we show the photoluminescence
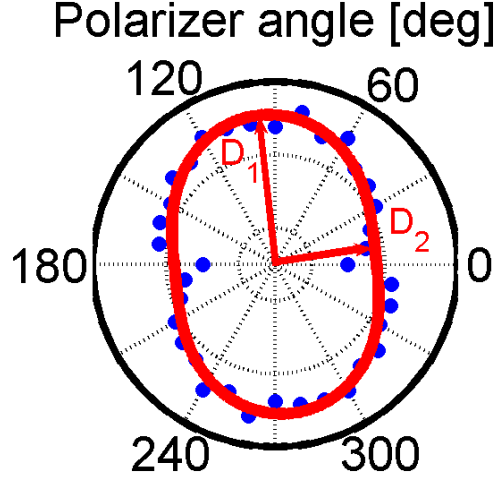

Figure S3: **Angular PL dependence.** Polarization angle dependence of the emitted photoluminescence (PL) of a hole-charged QD at 0 magnetic field. Blue dots: raw data; red curve: least squares fit of the elliptical polarization. The distance from the origin indicates the relative intensity of the emitted PL for a particular polarization angle. D_1 and D_2 are the main axes of the resulting elliptical polarization dependence (see text). Note that the data were taken for polarization angles between 0 and 180 degrees, and copied for the 180 - 360 degrees trajectory in view of the inversion symmetry of the system. The discontinuity at 0 degrees is a systematic experimental artifact.

(PL) as a function of applied bias voltage for a particular QD from a charge-tuneable device (above-band excitation, $\lambda = 785$ nm). A magnetic field of 6 T in Voigt geometry splits the transitions, and identification of the respective lines is made easier through the particular fine structure of transitions from charged and uncharged QDs [S5]. The charged QDs display a fourfold split of the PL for large magnetic field – see Fig. 1 **C**, where the magneto-PL of a hole-charged QD is shown (note that two of the four lines overlap due to limited spectrometer resolution, which can be seen as an apparent increase in brightness of the center line); it is this same particular signature that also allows us to identify the charged QDs in the δ-doped samples. The dependence on the pumping power allows us to separate excitonic emission lines from lines due to multi-excitonic complexes. The inhomogeneity in size and composition of the different QDs, together with the expected spectral line-up of the different charge states of a single QD, allow us to identify the lines in Fig. 1 **B**. As expected, increasing the QD bias leads to a transition from an uncharged to a charged state. However, and as reported in Ref. *S2*, we see a significant overlap between the respective voltage plateaus of the charged and uncharged QD state, which can be attributed to the relatively slow tunneling of the hole in our QDs. In addition, we notice that the exact position of the voltage plateaus depends on the amount of optical power used. Both above-band and resonant CW-excitation (as well as below-band modelocked (ML) laser pulses used for coherent spin rotations) can alter the bias voltage by as much as 0.1 - 0.2 V – we attribute this to residual absorption in the vicinity of the QD, which leads to the generation of charged carriers that can shift the QD energy ("DC"-Stark shift).

Finally, we characterized the fine structure of the QDs in our experiment. Without any magnetic field, the polarization of the emitted PL contains information about the hole spin eigenstates. In particular, strain and quantum dot asymmetry result in a small amount of HH-LH mixing. The resulting hole spin ground states $|\Uparrow\rangle$ and $|\Downarrow\rangle$ can be modeled as:

$$|\Uparrow\rangle = \left(\left|\Psi_{+3/2}\right\rangle + \beta^+ \left|\Psi_{-1/2}\right\rangle \right) / \sqrt{1 + |\beta|^2}$$
$$|\Downarrow\rangle = \left(\left|\Psi_{-3/2}\right\rangle + \beta^- \left|\Psi_{+1/2}\right\rangle \right) / \sqrt{1 + |\beta|^2}. \tag{S1}$$

Here, $\left|\Psi_{\pm 3/2}\right\rangle$ and $\left|\Psi_{\pm 1/2}\right\rangle$ represent the HH and LH states respectively. LH inmixing reflects itself in a slightly elliptical polarization of the hole-charged PL [*S6*]. We refer to Fig. SI-3.

The ratio, η, between the two axes of the elliptical polarization ($D_{1,2}$) is a measure for the amount of inmixing:

$$\eta = (\sqrt{3} - |\beta|)^2/(\sqrt{3} + |\beta|)^2. \tag{S2}$$

For the results presented in this Letter, the particular QD had a value of $\beta \sim 17\%$.

S.2. EXPERIMENTAL SETUP

For all experiments, the device is cooled to 1.6 K in a superconducting magnetic cryostat. For the charge-tuneable QDs, electrical contacts are attached to the front and the back of the device for biasing. The electrical bias is set at the center of the single-hole-charging voltage plateau. The magnetic field is oriented in the plane of the sample (Voigt geometry). For the data in this Report, the magnetic field was kept at 8 T (except for the photoluminescence data in Figs. 1**B**,**C**: 6 T). A 0.68 NA aspheric lens inside the cryostat allows for focusing of both the pump and rotation lasers on the device. Slip-stick piezo-electric positioners move and focus the device inside the cryostat. The single-photon PL is collected using the same lens, filtered by a double-grating monochromator, and detected with a single photon counting module. Cross-polarization is used in order to further suppress the scattered light. The optical pumping laser is modulated using a fiber-based electro-optic modulator (EOM), with an extinction ratio of approximately 4×10^4; while this extinction ratio limits the T_1-time to several 10s of μs due to residual optical pumping, this value is still almost two orders of magnitude slower than any coherence-decay process in our system, and can therefore be ignored. The rotation pulses are selected by means of free-space EOMs, which are double-passed in order to increase their extinction ratios to approximately 10^4-10^5. All modulators are controlled by an arbitrary data pattern generator, synchronized to the mode-locked laser. Relative delays between the pulses are changed by extending the path length of one arm of the Ramsey interferometer by moving a retroreflector on a motorized stage; we obtain large delays by moving the stage on a rail[$S7$]. The rotation laser is modulated at 1 kHz, and the signal is detected with a digital lock-in detector synchronized to this frequency. The photon counters are gated on only during the 26 ns optical pumping period in order to reduce dark counts.

S.3. COHERENT ROTATION PULSE MODEL

The effect of a broadband, detuned optical pulse on the hole spin ground states can be equivalently modeled as resulting from a stimulated Raman transition or as the result of an AC-Stark shift – we elaborate here on the latter interpretation [S8, S9]. As the pulse duration of 3.67 ps is much shorter than the Larmor precession frequency $\delta_{\mathrm{HH}}/2\pi = 30.2$ GHz, one can look at the interaction in the basis of the light pulse (z-basis as indicated in Fig. SI-4 **A**; note that this is not the eigenbasis of the spins in the absence of any light pulses – that is the x-basis in our convention). In this basis, the magnetic field results in an off-diagonal coupling between the hole spins, indicated by B_x in Fig. SI-4 **B**. However, given that the pulse is much faster than the Larmor-precession, the z-basis spins can be considered as effectively degenerate, and the magnetic field can be approximately neglected in the remainder of the analysis.

For perfect selection rules and ideally circularly polarized light pulses, only one of the z-basis hole spin states is coupled to the trion states; the other state is dark. For realistic quantum dots, imperfect selection rules and limited control over the exact polarization of the light pulse inside the cavity lead to both hole spin ground states being coupled to the trion states. The coupling strengths $\Omega_{1,2}$ are indicated in Fig. SI-4 **B**; typically, one is much larger than the other. For a detuning Δ (340 GHz in our case) larger than the pulse bandwidth, the pulse adiabatically mixes the hole spin ground state and its excited trion state. The effect of the time-dependent adiabatic mixing is a time-dependent AC-Stark-shift $\delta_{1,2}(t)$, given by:

$$\delta_{1,2}(t) = \frac{1}{2}\sqrt{\Delta^2 + |\Omega_{1,2}(t)|^2} - \frac{\Delta}{2}. \tag{S3}$$

A hole spin initialized in the x-basis due to the magnetic field can be written as a superposition of z-basis states with equal weight. The effect of the pulse is then to AC-Stark-shift these states by a different amount, leading to a net rotation angle θ and rotation pulse power (P_{rot}) dependent Rabi oscillations:

$$\theta = \int dt \left[\delta_1(t) - \delta_2(t) \right] = \frac{1}{2} \int dt \left[\sqrt{\Delta^2 + |\Omega_1(t)|^2} - \sqrt{\Delta^2 + |\Omega_2(t)|^2} \right]. \tag{S4}$$

Here, the integration is over the duration of a single rotation pulse. Fig. SI-4 **C** illustrates the predicted Rabi oscillations in this AC-Stark framework. The data show an incoherent

background ($\sim P_{\text{rot}}^{0.65}$) which is shown as the green curve in this figure. After subtracting the background, a least-squares fit extracted the amplitude of the Rabi oscillations. The pulse shape was modelled as Gaussian, with a measured FWHM of 3.67 ps, and for the detuning, the measured value of 340 GHz was used. The best fit was obtained for a ratio
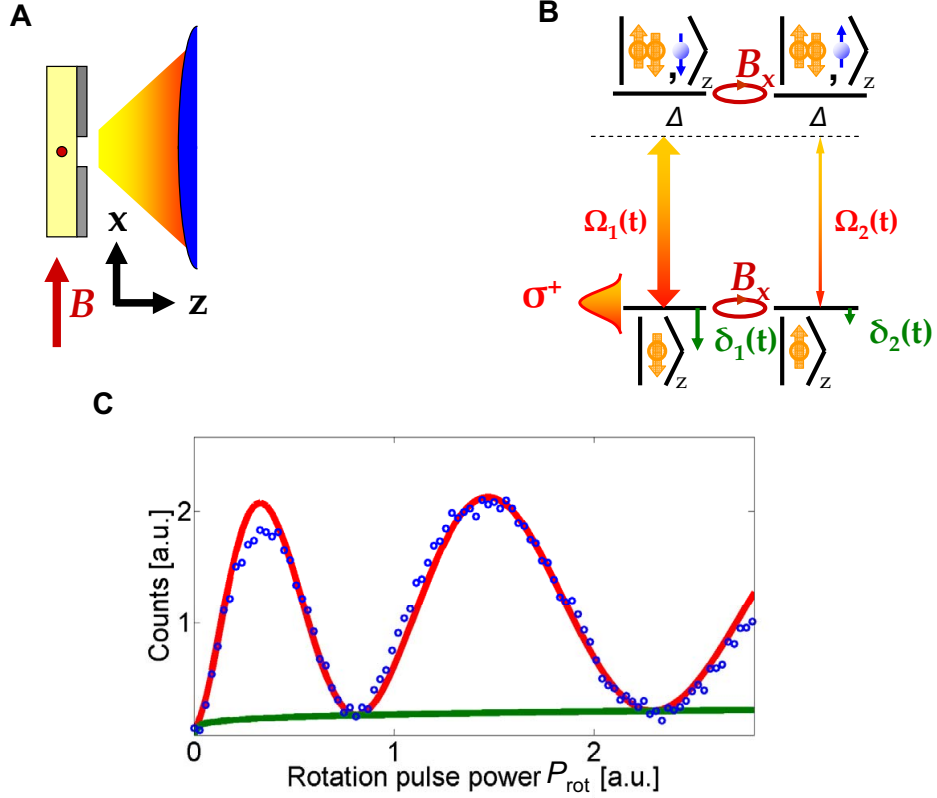

Figure S4: **Coherent rotation modelling.** (**A**) Geometry and axis convention used in the experiment. The magnetic field is oriented along x, while the laser pulse is aligned to the growth direction z. (**B**) AC-Stark shift in the Z-basis: $|\Downarrow\rangle$ and $|\Uparrow\rangle$ are the hole spin ground states, while $|\Downarrow\Uparrow,\downarrow\rangle$ and $|\Downarrow\Uparrow,\uparrow\rangle$ represent the trion states. Δ represents the detuning, and the circularly polarized laser pulse couples the ground states to the excited states ($\Omega_{1,2}(t)$), resulting in AC-Stark shifts $\delta_{1,2}(t)$. (**C**) Rabi oscillations fit through the AC-Stark model. Blue circles: raw data; red: AC-Stark shift predicted Rabi oscillations, on top of an incoherent background (green).

$|\Omega_1(t)|^2/|\Omega_2(t)|^2 = 3.7$, and is indicated by the red curve. The model fits the data very well, with the exception of the height of the first peak. This deviation can be attributed to the still finite duration of the laser pulse, and our neglecting the Larmor precession in this model. In Ref. *S10* we demonstrated how the combined effect of Larmor precession and pulse-induced Rabi oscillations leads to an effective rotation axis that is in between the laser pulse (z-axis) and the magnetic field axis (x), leading to a reduced height of the first π pulse. A full master equation solution can qualitatively reproduce this reduced height. The incoherent background and upward trend, however, cannot be reproduced by solving the full master equation. Its origin is currently unknown, although it might be related to a change in the optimum bias position of the QD for high rotation pulse powers as reported above.

S.4. ROTATION PULSE FIDELITY

We model the fidelity of a $\pi/2$ pulse using the same methods as described in Ref. *S10*. We assume that the Bloch vector after optical pumping starts with length L_0, and shrinks by a factor $D_{\pi/2}$ after a single $\pi/2$ pulse. The combined effect of two $\pi/2$ pulses separated by a variable Larmor precession delay τ is that the population in $|\Uparrow\rangle$ oscillates between $(1+L_0 D_{\pi/2}^2)/2$ and $(1\text{-}L_0 D_{\pi/2}^2)/2$ with period $2\pi/\delta_{\mathrm{HH}}$. We use a digital lock-in procedure which automatically subtracts a background of $(1\text{-}L_0)/2$, leading to a net oscillation between $(L_0+L_0 D_{\pi/2}^2)/2$ and $(L_0\text{-}L_0 D_{\pi/2}^2)/2$. With a scaling factor C connecting population in $|\Uparrow\rangle$ to the measured counts, the resulting signal oscillates between $CL_0(1+D_{\pi/2}^2)/2$ and $CL_0(1\text{-}D_{\pi/2}^2)/2$.

From the sinusoidal fit to the $\pi/2$ Ramsey fringes in Fig. 2 **D**, we obtain a value for $D_{\pi/2}$ of 0.89, which implies a fidelity $F_{\pi/2} = (1 + D_{\pi/2}) = 0.945$ as quoted in the main text. This value is comparable to currently achieved values for electron spins ($F_{\pi/2} = 0.94$ as previously reported in Ref. *S10*, subsequently slightly improved to about 0.97 by the incorporation of a microcavity and optimized detuning, see for example Fig. 1 **D** in Ref. *S7*). The fidelity is limited by the incoherent population, which can be seen in Fig. SI-4 **C**.

A similar analysis method can be used for different pulse angles, and yields similar fidelities. For different dots, different fidelities are obtained, but are consistently found to be upwards of 0.9, limited by the incoherent population induced by the optical rotation pulse.

S.5. ELECTRON SPIN-NUCLEAR FEEDBACK

For an electron-charged QD, a simple and mathematically tractable nonlinear diffusion equation was derived in Ref. *S11*, describing the nonlinear feedback loop resulting from nuclear-dependent Larmor precession (Overhauser shift) and electron-spin dependent nuclear spin relaxation. This model can be extended to incorporate the hysteretic and asymmetric curves obtained while scanning through the optical resonance frequency of the QD (the $|\downarrow\rangle$-$|\downarrow\uparrow, \Uparrow\rangle$ transition, see Fig. 3 **C**).

The devices used for the electron spin-nuclear feedback experiments have been extensively described in Refs. *S7*, *S11*. They consist of self-assembled InAs QDs (density: roughly 2×10^9 cm^{-2}), with a Si δ-doping layer 10 nm below the QDs for stochastic QD charging (roughly 1 in 3 QDs were charged). The QDs were embedded in a one-sided planar microcavity ($Q \sim 200$) consisting of 24 respectively 5 AlAs/GaAs $\lambda/4$ layers.

S.5.1. Hysteretic and asymmetric electron spin Ramsey fringes

For a single electron spin in a QD, the strong contact hyperfine interaction makes the electron spin Larmor precession frequency very sensitive to the net polarization of the nuclear spin bath through the Overhauser shift. Conversely, in Ref. *S11* it was shown that the evolution of the nuclei in the quantum dot depends on the rate of trions being generated – the unpaired hole in the electron spin trion state allows for quasi energy-conserving nuclear spin flips to occur. This effect, together with background nuclear spin diffusion, can be modelled as a nonlinear diffusion equation for the average Overhauser shift ω:

$$\frac{\partial \omega}{\partial t} = -\kappa\omega + \alpha\frac{\partial C(\omega, \tau)}{\partial \omega}, \tag{S5}$$

where $C(\omega, \tau)$ is the trion generation rate in the experiment. For Ramsey fringes, $C(\omega, \tau)$ can be calculated by analyzing the pulse pattern (see Fig. SI-5 **B**, inset). In particular, a CW optical pumping pulse is interspersed with two $\pi/2$ rotation pulses, separated by a variable delay τ. Denoting the average spin polarization by S, the spin-up probability by P($\uparrow$) (equal to $(1 + S)/2$) and the spin-down probability by P($\downarrow$), we can relate the spin polarization S_{after} right after optical pumping for a time T to the polarization S_{before} before the arrival of the optical pumping pulse:
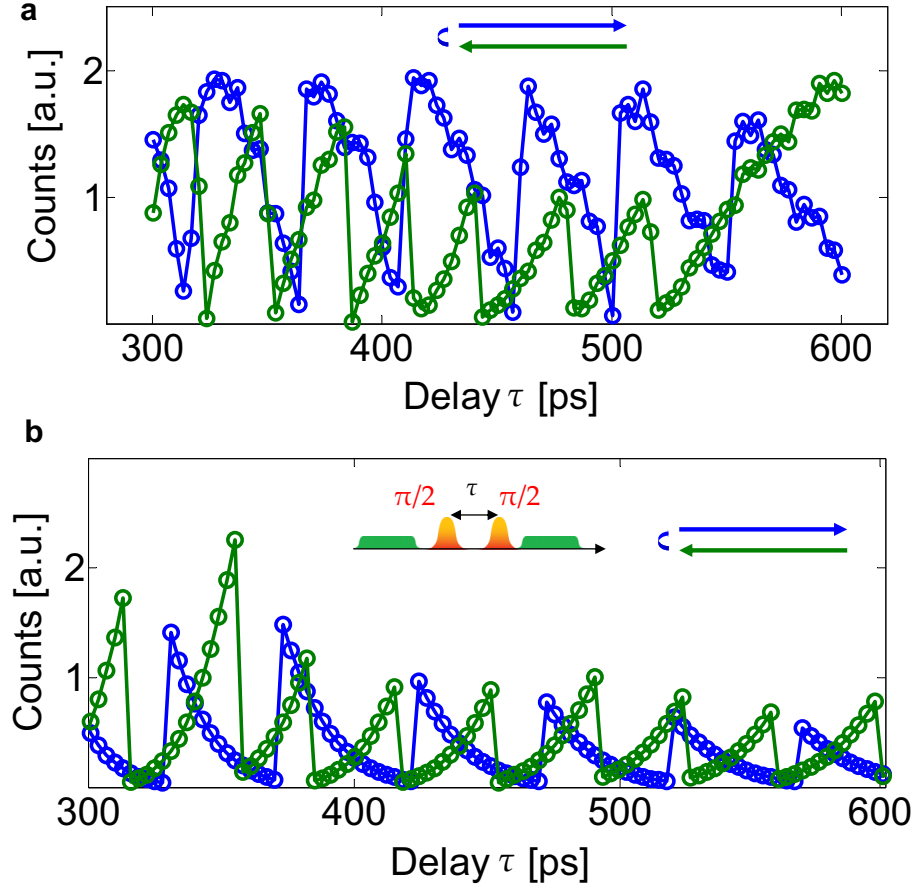
11

Figure S5: **Electron spin Ramsey fringe hysteresis.** (**A**) Asymmetric and hysteretic Ramsey fringes for an electron spin (measured; from Ref. *S11*). The green and blue arrows indicate the scanning direction of the pulse delay τ. (**B**) Asymmetric and hysteretic electron spin Ramsey fringes as predicted by the model in Ref. *S11*. Inset: scan direction and pulse timing.

$$
\begin{aligned}
S_{\text{after}} &= \sum_{m=\uparrow,\downarrow} \left[\frac{1}{2} P(\uparrow|m) P_{\text{before}}(m) - \frac{1}{2} P(\downarrow|m) P_{\text{before}}(m) \right] \\
&= \frac{(1 - e^{-\beta(\omega)T})}{2} + S_{\text{before}} e^{-\beta(\omega)T}.
\end{aligned}
\tag{S6}
$$

Here, $\beta(\omega)$ represents the optical pumping/absorption profile, assumed to be Gaussian. In addition, the interference of the two $\pi/2$ rotation pulses separated by a delay τ yields:

$$S_{\text{before}} = -\cos((\omega_0 + \omega)\tau)S_{\text{after}}, \tag{S7}$$

where ω_0 represents the Larmor precession in the absence of any Overhauser effects. Together, this results in a trion generation rate $C(\omega, \tau)$:

$$
\begin{aligned}
C(\omega, \tau) &= S_{\text{after}} - S_{\text{before}} \\
&= \frac{1}{2} \frac{(1 - e^{-\beta(\omega)T})\{1 + \cos[(\omega_0 + \omega)\tau]\}}{1 + \cos[(\omega_0 + \omega)\tau]e^{-\beta(\omega)T}}.
\end{aligned}
\tag{S8}
$$

Eq. 5 is derived by invoking a separation of timescales [S11], and can be solved to yield steady-state solutions $\omega_{\text{f}}(\tau)$. The integration times used in the experiment (few seconds for each different value of τ) were found to be sufficient for reaching these steady-state solutions. Due to the nonlinearity, the solutions depend on the initial conditions, and therefore on the direction in which τ is varied. Figs. SI-5 **A** and **B** compare the experimentally obtained Ramsey fringes with those obtained by numerically solving eq. 5. In Fig. SI-5 **B**, $\beta(\omega)$ was assumed to be Gaussian ($\beta_0 e^{-(\omega^2/2\sigma^2)}$ with $\sigma/2\pi = 1.6$ GHz), $\kappa = 10$ s^{-1} and $\kappa/\alpha = 10^4$ ps^2.

S.5.2. Hysteretic and asymmetric electron spin CW resonance scanning

In Refs. *S12*, *S13* hysteretic effects were observed while scanning a narrowband CW laser through the QD optical resonance frequency. In Ref. *S13*, a single electron-charged QD was studied using Coherent Population Trapping in Voigt geometry. In order to avoid optical pumping into one of the electron spin ground states, one laser was kept fixed, while another laser was scanned through the QD resonance wavelength. Trion-induced nuclear spin flips lead to a dragging of the resonance wavelength upon scanning the laser frequency – and the consequent hysteresis.

A similar effect was observed for a single electron-charged QD in our system. Instead of having two narrowband lasers, a π rotation pulse was used to compensate for optical pumping, and a narrowband CW-laser (few MHz linewidth) was scanned through the QD resonance wavelength ($|\downarrow\rangle$-$|\downarrow\uparrow, \Uparrow\rangle$-transition [S11]). Fig. SI-6 **A** illustrates the hysteresis and asymmetry upon scanning the CW-laser in different directions (scan speed: between 10 and 200 MHz per second - the same values were systematically studied for electron and hole spin experiments).
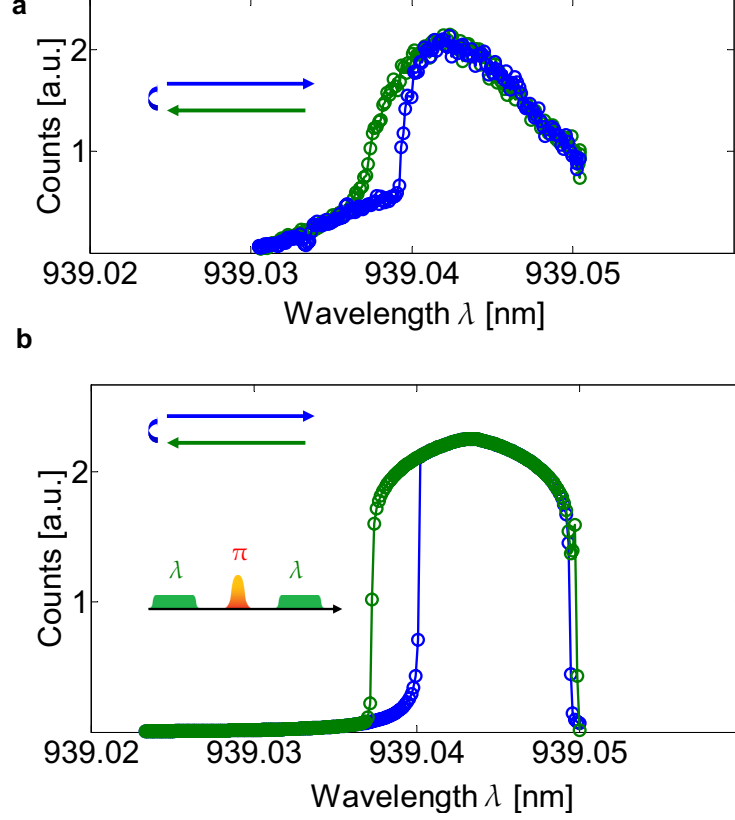
Figure S6: **Electron spin resonant scanning hysteresis.** (**A**) Asymmetric and hysteretic resonance scan for an electron spin (experimental). The green and blue circles indicate the wavelength scanning direction. (**B**) Asymmetric and hysteretic electron spin resonance scan, as predicted by an extension of the model in Ref. *S11*. Inset: scan direction and pulse timing.

Eq. 5 can again be used to model the Overhauser shift ω. The difference with the Ramsey fringe hysteresis lies in the trion generation rate $C(\omega, \omega_{\text{las}}, \theta)$, where ω_{las} stands for the laser frequency, and θ for the rotation angle of the single pulse used in the experiment (π in our case). The pulse sequence used is shown in Fig. SI-6 **B**, inset. After optical pumping for a time T, we still have that

$$S_{\text{after}} = \frac{(1 - e^{-\beta(\omega, \omega_{\text{las}}, \omega_{\text{res}})T})}{2} + S_{\text{before}} e^{-\beta(\omega, \omega_{\text{las}}, \omega_{\text{res}})T}, \tag{S9}$$

where ω_{las} and ω_{res} respectively stand for the laser frequency and the QD resonance frequency in the absence of nuclear spin effects. However, the single rotation pulse with angle θ has now a different effect on the spin polarization:

$$S_{\text{before}} = \cos(\theta)S_{\text{after}}. \tag{S10}$$

This results in a net trion generation rate $C(\omega, \omega_{\text{las}}, \theta)$:

$$
\begin{aligned}
C(\omega, \omega_{\text{las}}, \theta) &= S_{\text{after}} - S_{\text{before}} \\
&= \frac{1}{2}\frac{(1 - e^{-\beta(\omega,\omega_{\text{las}},\omega_{\text{res}})T})[1 - \cos(\theta)]}{1 - \cos(\theta)e^{-\beta(\omega,\omega_{\text{las}},\omega_{\text{res}})T}}.
\end{aligned} \tag{S11}
$$

We can again obtain steady-state values ω_f from Eq. 5. Whether or not steady state is obtained, however, depends critically on the scan speed – a dependence we also notice experimentally. We assume a Lorentzian QD linewidth ($\beta(\omega) = \beta_0/(1+(\omega_{\text{las}}-\omega_{\text{res}}-\omega)^2/\sigma^2)$, $\sigma/2\pi = 200$ MHz) – other lineshapes (Gaussian, Voigt) yield qualitatively similar results. While the exact resulting lineshape depends critically on the intial conditions and details of the QD and experiment (initial Overhauser shift ω_0, scan speed, lineshape, etc.), the qualitative features are well reproduced in this model: Fig. SI-6 **B** shows the numerical solution to Eq. 5. κ is estimated as 8.5 s^{-1}, and $\kappa/\alpha = 2.8{\times}10^4$ ps^2.

S.6. NUCLEAR FEEDBACK: COMPARISON BETWEEN ELECTRON AND HOLE SPINS

For the hysteretic effects of a single electron spin coupled to the nuclear spins in the QD, the average Overhauser contribution to the Larmor precession frequency can be extracted from the model described above. Fig. SI-7 **A** shows the Overhauser shift for the hysteretic Ramsey fringes described above. As our model captures only the average Overhauser shift [S9, S11], one conservative way of estimating the error on the obtained values is to assume that there is no narrowing of the nuclear spin distribution due to the development of nuclear spin polarization [S11]. In that case, the T_2^* value of 1.71 ns obtained in Ref. S7 can be used to estimate the variance on the Overhauser shift due to time-ensemble effects, yielding $\sigma_\omega/2\pi = \sqrt{2}/(2\pi \times T_2^*) = 130$ MHz. We can therefore estimate the maximum Overhauser shifts for a single electron spin due to the interaction with the nuclei at
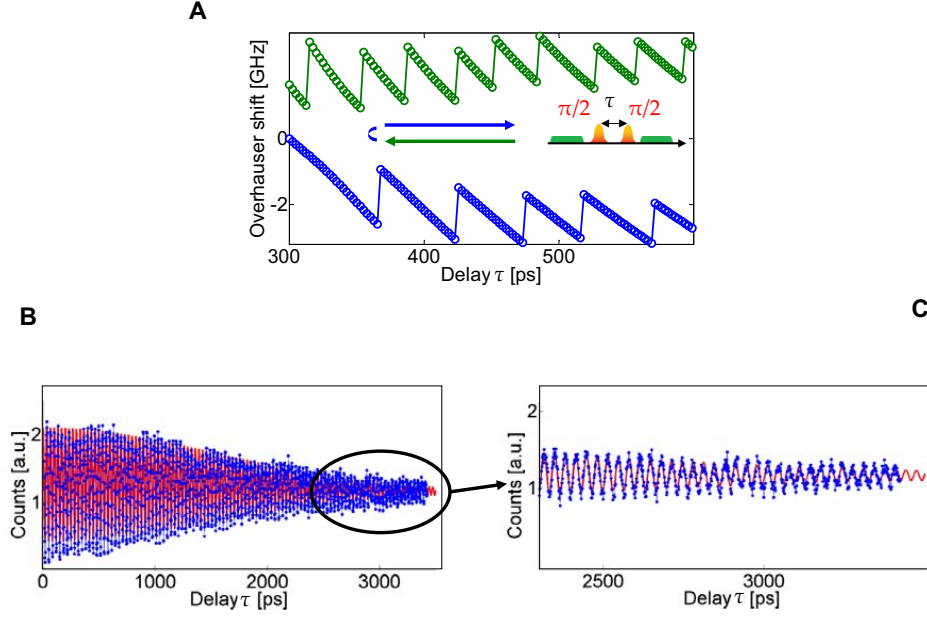
15

Figure S7: **Electron and hole spin Overhauser shifts compared.** (**A**) Modeled average Overhauser shift for hysteretic Ramsey fringes of a single electron spin; the green and blue circles indicate the wavelength scanning direction, as indicated by the arrows. (**B**) Time-averaged dephasing of a single hole spin; blue: raw data, red: fit to a sinusoid with Gaussian envelope. No variance of the average Overhauser shift was observed. (**C**) Zoomed-in version of (**B**) – note that the phase of the fringes remains constant over the entire scan range.

3 ± 0.13 GHz. The resonance scan model predicts a similar, or slightly reduced, maximum Overhauser shift.

A single hole spin does not display any hysteresis or nonlinearity in either the Ramsey fringe or resonance scanning experiment (the same range of CW laser scan speeds and integration times was examined for both the electron and hole samples). Moreover, compared to the indirect method of extracting Overhauser shifts through modelling based on eq. 5, a more accurate estimate of the Overhauser shift can be obtained from the phase of the Ramsey fringes. That phase equals $(\omega_0+\omega)\tau$, and the Ramsey fringes are shown in Figs. SI-7 **B** and **C**, together with a sinusoidal fit with Gaussian envelope (red curve). The raw data hardly deviate from the fit, except for very long delays, where noise effects dominate. Even

with the noise, the deviation is at most 0.5 - 1 radians for a total delay τ of 3.5 ns, leading to a maximum Overhauser shift $\omega/2\pi$ of 40±100 MHz. We may bound any possible hole Overhauser shifts by supposing they are masked by experimental noise. Here, the width of the time-averaged Larmor precession frequency distribution leading to T_2^*-decay results in an uncertainty $\sigma_\omega/2\pi = \sqrt{2}/(2\pi \times T_2^*) = 100$ MHz, using our experimentally observed T_2^* value of 2.3 ns. We emphasize that this is a worst-case estimate, for the case in which nuclear effects would limit the time-averaged dephasing, which we consider unlikely.

Comparing these two values, we see that the developed Overhauser shift for the hole spin is at least 30 times smaller than that for the electron spin, where the factor of 30 is limited by experimental noise and T_2^* effects of the hole spin. While the Overhauser shift depends both on the developed nuclear spin polarization and the sensitivity of the hole spin to that nuclear spin polarization, this significant reduction of the measured Overhauser shift dramatically illustrates the suppression of feedback effects between the nuclear spin bath and the hole spin.

S.7. COHERENCE DECAY OF THE HOLE QUBIT

The time-averaged dephasing data in Figs. 4 **A** and **B** were obtained by moving a motorized stage on a rail. For each rail position, the motorized stage was scanned, resulting in a relative delay τ_{rel} (varying between 0 and 270 ps) between the two $\pi/2$ pulses. The distance between subsequent rail position was 270 ps. For each rail position, the resulting Ramsey fringes were fit to a sinusoid, where the amplitude, offset, period and phase were used as fit parameters. The resulting fringe heights are plotted in Fig. 4 **B**, and are best fit to a Gaussian. A slight upward trend can be observed in Fig. 4 **A**, due to an increased incoherent background and/or slight deviations from the ideal $\pi/2$ pulse angle.

A similar procedure was used for the spin echo data in Figs. 4 **E** and **F**. Here, the position of the motorized stage on the rail was kept fixed; however, a coarse delay was added by having the EOMs pick pulses with a delay of 13 ns or multiples thereof (see Fig. 4 **E**, inset: $2T$ is a multiple of 13 ns). For each value of $2T$, echo fringes were obtained when scanning the middle π pulse. The fringes were fit to a sinusoid, and the fringe heights are shown in Fig. 4 **F**. Here, the best fit to the fringe heights is obtained by an exponential.

In comparing δ-doped and charge-tuneable devices, we obtained qualitatively and quan-

titatively similar values, in particular, T_2^*-values of a few ns, and T_2-times of at least several hundred ns.

[S1] J. M. García, T. Mankad, P. O. Holtz, P. J. Wellman, and P. M. Petroff, Appl. Phys. Lett. **72**, 3172 (1998).

[S2] B. D. Gerardot et al., Nature **451**, 441 (2008).

[S3] D. Brunner, B. D. Gerardot, P. A. Dalgarno, G. Wst, K. Karrai, N. G. Stoltz, P. M. Petroff, and R. J. Warburton, Science **325**, 70 (2009).

[S4] http://www.nextnano.de/.

[S5] M. Bayer et al., Phys. Rev. B **65**, 195315 (2002).

[S6] T. Belhadj et al., Appl. Phys. Lett. **97**, 051111 (2010).

[S7] D. Press, K. De Greve, P. McMahon, T. D. Ladd, B. Friess, C. Schneider, M. Kamp, S. Hfling, A. Forchel, and Y. Yamamoto, Nat. Photonics **4**, 367 (2010).

[S8] J. Berezovsky, M. H. Mikkelson, N. G. Stoltz, L. A. Coldren, and D. D. Awschalom, Science **320**, 349 (2008).

[S9] T. D. Ladd *et al.*, arXiv:1008.0912v1 (2010) (to appear in Proc. SPIE).

[S10] D. Press, T. D. Ladd, B. Zhang, and Y. Yamamoto, Nature **456**, 218 (2008).

[S11] T. D. Ladd, D. Press, K. De Greve, P. McMahon, B. Friess, C. Schneider, M. Kamp, S. Höfling, A. Forchel, and Y. Yamamoto, Phys. Rev. Lett. **105**, 107401 (2010).

[S12] C. Latta et al., Nat. Phys. **5**, 758 (2009).

[S13] X. Xu et al., Nature **459**, 1105 (2009).